

Stability analysis for fast ion driven instabilities in stellarators using a particle/wave transfer approach

Donald A. Spong (*Oak Ridge National Laboratory*), email: sponгда@ornl.gov

Axel Könies (*IPP- Greifswald*), email: axel.koenies@ipp.mpg.de

Abstract

Stellarators and tokamaks with 3D effects provide unique challenges for the stability analysis of energetic particle driven Alfvén instabilities. First, due to the presence of both toroidal and poloidal equilibrium couplings, the Alfvén gap mode structures and continuum couplings are more complex than for 2D equilibria. Also, the fast ion orbit deviations from flux surfaces are generally larger than in the case of tokamaks. To address these issues, a δf particle-based approach has been developed that evaluates linear growth rates for such instabilities by accumulating the wave/particle energy transfers between a prescribed ideal MHD Alfvén eigenmode (e.g., obtained using the AE3D spectral eigenmode code) and a large collection of particles following their unperturbed orbits. This is currently a perturbative model, but inherently includes finite guiding center orbit deviations from flux surfaces for passing, trapped and transitional particle populations. Benchmarks have been made against axisymmetric calculations, indicating the effects of finite orbit width stabilization as $\rho_{\text{fast}}/\langle a \rangle$ is increased. The calculation is global, readily parallelized and has been tested using several million particles. Besides providing linear growth rates, it is also useful for understanding the location of the particle-wave resonances in 3D systems and as a test-bed for particle loading and evolution techniques for nonlinear models

Introduction

Energetic particle destabilized Alfvén instabilities have been observed in a range of stellarators, including W7-AS¹, CHS², LHD³, TJ-II⁴, Heliotron-J⁵, and HSX⁶. The Alfvén gap structure of stellarators shares common modes with the tokamak, such as the toroidal, reversed shear and global Alfvén eigenmodes (TAE, RSAE and GAE) and introduces several new modes (helical and mirror Alfvén eigenmodes – HAE, MAE) that are unique to three-dimensional configurations. An additional issue that will influence the stability properties of resonantly destabilized Alfvén modes for stellarators is the displacement of energetic particle orbits off of flux surfaces. This displacement is generally larger than that for axisymmetric devices, where the conservation of the canonical angular momentum (P_ϕ) limits orbit deviations away from flux surfaces. Finite orbit width (FOW) effects on Alfvénic instabilities have been extensively analyzed for tokamaks^{7,8,9,10,11,12,13,14,15} and generally decrease the growth rates by a factor of the order^{7,9} Δ_m/Δ_b , where Δ_m is the mode width and Δ_b is a typical orbit displacement width (i.e., a banana width for trapped particles). This stabilization arises due to the fact that if only a fraction of the orbit trajectory intersects the region where the Alfvén mode structure is dominant, then this will cause the strength of the wave-particle resonance to be proportionally reduced¹². It has also

been noted that there could be regimes where FOW effects can have destabilizing influences, such as for fast ions born near the magnetic axis.¹² The drift trajectories of such ions could cause them to sample Alfvénic mode regions further out in minor radius from their starting locations. Also, calculations have reported⁸ that FOW effects on passing particles with $v_{\text{fast}}/v_A < 1$ can be destabilizing in tokamaks.

FOW effects on Alfvén instabilities in stellarators have mostly been considered analytically to date, with applications to W7-AS¹⁶. In this case, it was concluded that FOW effects should generally reduce Alfvén growth rates, although it was noted that there could be some regimes where FOW effects might introduce new resonances that would enhance instability¹⁶.

This paper describes a new computational method for addressing FOW effects on Alfvén instabilities in stellarators, based on a δf particle-based approach. This is a perturbative wave-particle energy transfer method based on stable 3D reduced MHD Alfvén eigenmodes, as can be provided by codes such as CAS3D¹⁷ or AE3D¹⁸. These codes use VMEC equilibria so a range of different stellarator and shaped cross section tokamak configurations can be addressed. Also, a range of different Alfvén mode structures can be analyzed; here example applications for TAE, GAE and HAE modes will be presented. Finally, since the full guiding center particle trajectories are followed, there are no approximations made related to the ratio of the mode width to the particle orbit width. Also, all particle populations (trapped, passing, transitional) are consistently included.

Analysis

As mentioned above, a perturbative approach is used, based on a decomposition of the kinetic energy variational form into MHD and energetic particle (EP) components. For our ideal MHD model, we can show that:

$$\frac{\partial}{\partial t} W_{fMHD} = \frac{\partial}{\partial t} \left\{ \frac{1}{2} \int d^3x \frac{Mn}{B^2} (\nabla_{\perp} \phi)^2 + \frac{1}{2\mu_0} \int d^3x (\nabla_{\perp} A_{\parallel})^2 \right\} = 0 \quad (1)$$

i.e., the energy of the electromagnetic field is conserved. In the case of an interacting energetic particle species, we know that

$$W_{field} = \frac{1}{2} \int d^6z B_{\parallel}^* q \left\langle \phi - \frac{P_{\parallel}}{M} A_{\parallel} \right\rangle f \quad (2)$$

and if the system is governed by MHD then $W_{fMHD} = W_{field}$ should hold, and

$$\frac{\partial W_{fMHD}}{\partial t} = \frac{\partial W_{field}}{\partial t}. \text{ We can then write } \frac{\partial W_{fMHD}}{\partial t} \text{ as follows:}$$

$$\frac{\partial W_{fMHD}}{\partial t} = q \int d^6 z B_{\parallel}^* f \bar{\mathbf{R}} \cdot \bar{\nabla} \left\langle \phi - \frac{p_{\parallel}}{M} A_{\parallel} \right\rangle + q \int d^6 z \bar{b}^* \cdot \bar{\nabla} \mu B \frac{A_{\parallel}}{M} B_{\parallel}^* f \quad (3)$$

This problem can now be solved in frequency space, based on the argument that energy $\propto \phi^2 \sim e^{2\gamma t}$, resulting in:

$$\gamma \simeq \frac{\langle \bar{\mathbf{J}} \cdot \bar{\mathbf{E}} \rangle}{2W_{fMHD}} \quad (4)$$

The growth rate can be written more specifically as:

$$\gamma = \frac{Ze \int d^6 z B_{\parallel}^* \delta f \left[\dot{\mathbf{R}}^{(0)} \cdot \nabla (\phi - v_{\parallel} A_{\parallel}) + M^{-1} A_{\parallel} \hat{b}^* \cdot \mu \nabla B \right]}{\int d^3 x \left\{ \frac{Mn}{B^2} |\nabla_{\perp} \phi|^2 + \frac{1}{\mu_0} |\nabla A_{\parallel}|^2 \right\}} \quad (5)$$

As indicated in Equation (5), the growth/damping is physically related to the magnitude and direction of the wave-particle energy transfers through the summation of $\mathbf{J}_{EP} \cdot \mathbf{E}$ increments over the particle population. To evaluate Equation (5), the first order distribution function is required. This is obtained by expanding drift-kinetic equation about the unperturbed distribution (i.e., the portion not including the time-varying fields of the Alfvén eigenmode) as follows:

$$\text{distribution function: } f = f(\varepsilon, \mu, s, t) = f_0 + \delta f \quad (6)$$

$$\left(\frac{\partial}{\partial t} + \dot{\mathbf{R}}^{(0)} \cdot \bar{\nabla} \right) \delta f = - \left(\dot{\mathbf{R}}^{(1)} \cdot \bar{\nabla} f_0 + \dot{\varepsilon}^{(1)} \frac{\partial f_0}{\partial \varepsilon} \right) \quad (7)$$

$$\dot{\varepsilon}^{(1)} = Ze \frac{\partial}{\partial t} \left(\phi - \frac{p_{\parallel}}{M} A_{\parallel} \right); \quad \dot{\mu} = 0 \quad (8)$$

$$\dot{\mathbf{R}}^{(1)} \cdot \bar{\nabla} f_0 \simeq - \frac{\hat{b} \times \bar{\nabla} f_0}{ZeB} \cdot \bar{\nabla} \left[Ze \left(\phi - \frac{p_{\parallel}}{M} A_{\parallel} \right) \right] \quad (9)$$

This results in the following equation for δf :

$$\frac{d}{dt} \delta f = \left[\frac{\hat{b} \times \vec{\nabla} f_0}{ZeB} \cdot \vec{\nabla} - \frac{\partial f_0}{\partial \varepsilon} \frac{\partial}{\partial t} \right] \left[Ze \left(\phi - \frac{p_{\parallel}}{M} A_{\parallel} \right) \right] \quad (10)$$

The above equation can be solved by integrating along the characteristics of the left-hand side, i.e., the unperturbed particle orbits. The inhomogeneous term on the right-hand side of Equation (10) is taken into account using particle weight functions, as indicated below:

$$w = \frac{\delta f}{g}; \quad \dot{w}_i = - \left[\frac{f(t=0, z=z_i)}{g(t=0, z=z_i)} - w_i \right] \frac{1}{f} \frac{df}{dt} \quad (11)$$

where

$$\frac{1}{f} \frac{df}{dt} \approx \frac{1}{G + \pm I} \left[\frac{n'}{n} + \frac{T'}{T} \left(\frac{mv^2}{2T} - \frac{3}{2} \right) \right] \left[\left(G \frac{\partial}{\partial \theta} - I \frac{\partial}{\partial \zeta} \right) (\phi - v_{\parallel} A_{\parallel}) \right] + \frac{Ze}{T} \frac{\partial}{\partial t} (\phi - v_{\parallel} A_{\parallel}) \quad (12)$$

The Alfvén eigenmode fields ϕ and A_{\parallel} are included by using a complex Fourier representation for their time plus poloidal/toroidal angle dependencies; the radial dependence is interpolated on a grid:

$$\phi, A_{\parallel} = \sum_{m,n} \left[\phi_{mn}(\rho), A_{\parallel mn}(\rho) \right] e^{\gamma_0 t} e^{i(m\theta - n\zeta - \omega_r t)}$$

This representation results in two weight equations (real and imaginary components) for each particle. Carrying along the two weights allows purely oscillating terms to be filtered out and only growing terms to be retained when the growth rate [Equation (5)] is evaluated. Typically, for the cases considered here, 30 to 100 (m,n) pairs are included in the above summation. As indicated, a finite (small) growth rate (γ_0) is allowed in the driving ϕ and A_{\parallel} fields in addition to the oscillating component (ω_r).

In evolving such a time domain model for Landau growth/damping effects, this artificial growth was included to avoid strongly resonant singular behavior (i.e., analogous to the frequency domain technique of deforming contours into the complex plane around singularities). It is then removed from the weight functions, before the instability growth is calculated. For the examples given in this paper, γ_0 has been set to zero, since the normal +/- variation of the resonant energy exchanges along the orbits has proven significant enough to avoid strongly resonant effects.

The initial particle distribution function used here has generally been taken as uniform in the five-dimensional phase space ($\rho, \theta, \zeta, \varepsilon, \mu$), except for the special case of beam distributions where only particles with $\mu / \varepsilon = 0$ have been used. Specific profiles and

velocity space distributions are then applied through appropriate choice of the $f(t=0)/g(t=0)$ factor in the weight evolution equation.

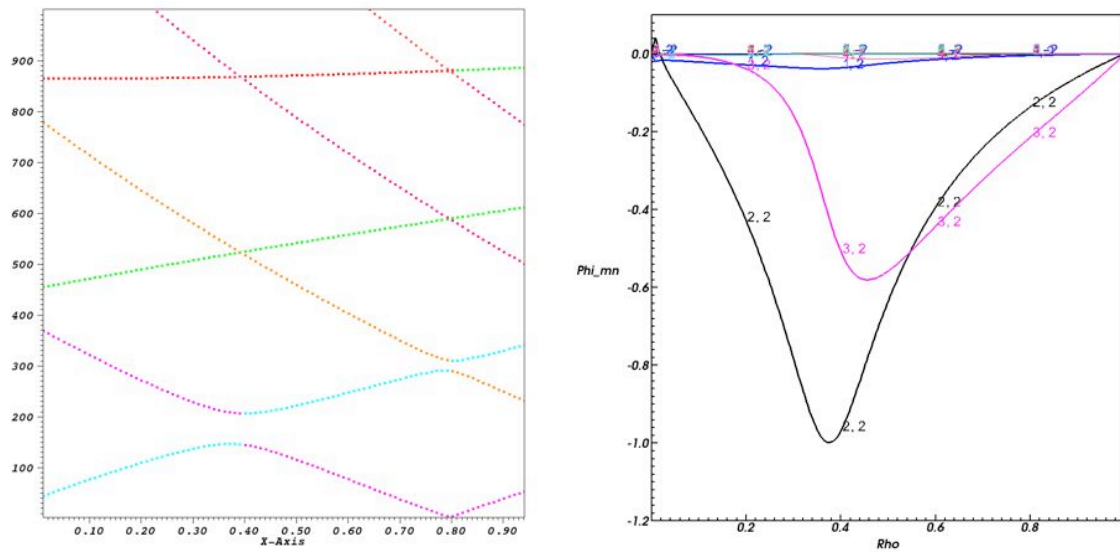


Figure 1 – (a) $n = 2$ continuum gap structure, and (b) radial eigenmode structure for a TAE occurring in the lowest open gap at 162 kHz.

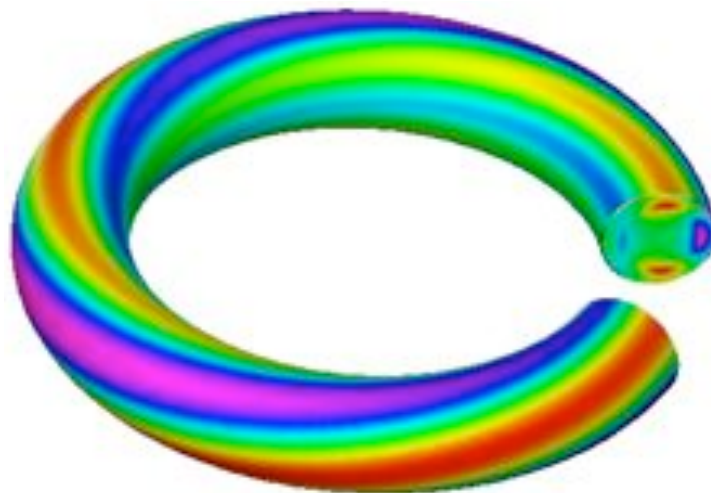


Figure 2 – TAE eigenmode structure projected onto an outer flux surface.

Axisymmetric benchmark case

This model was first applied to a tokamak benchmark case, for which growth rate results from several other codes were available. This exercise has proven quite valuable for correcting initial errors in the code, verifying the velocity and real space Jacobians, normalization factors, required number of particles and maximum cutoff energy in the particle distribution function.

This benchmark case is based on a tokamak with aspect ratio $R_0/a = 4.4$, $R_0 = 4$ meters, $\langle B \rangle = 5$ Tesla, $q(0) = 1.05$, $q(\text{edge}) = 1.65$, deuterium ions, constant ion density at $5 \times 10^{19} \text{ m}^{-3}$, and a Maxwellian/isotropic fast ion distribution function. An $n=2$ TAE mode was selected with a frequency of 162 kHz. The associated continuum gap structure and radial eigenmode structure are displayed in Figure 1. The

corresponding eigenmode structure projected onto an outer flux surface is shown in Figure 2.

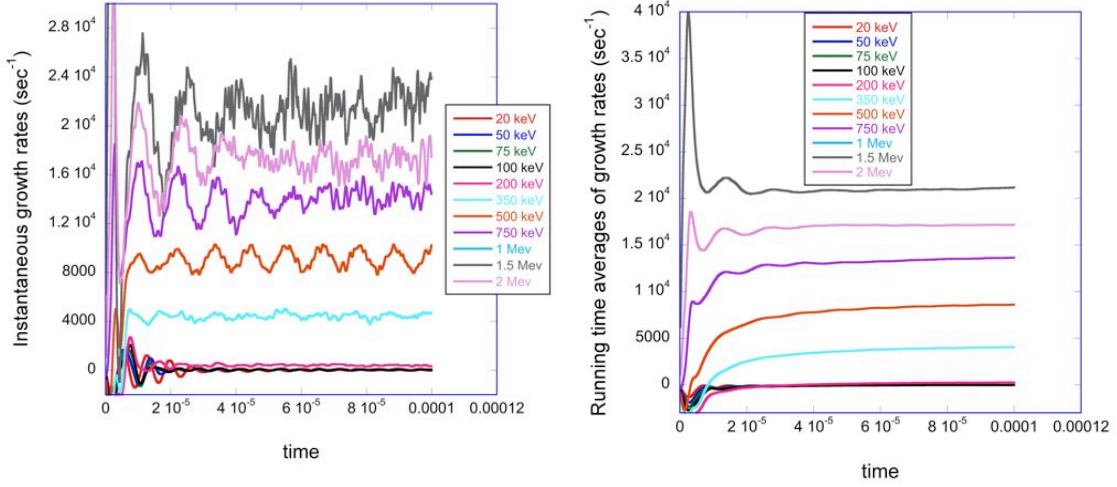


Figure 3 – (a) Instantaneous growth rates vs. time, and (b) growth rates vs. time after running time averages are applied.

For this case 10^6 marker particles were used with a centrally peaked fast ion density profile and $n_{\text{fast}}(0) = 1.2 \times 10^{18} \text{ m}^{-3}$. Fast ion density and other profiles used in these calculations are shown in Appendix A. Instantaneous and time averaged growth rates are given in Figure 3 for a range of particle energies. As can be seen, the growth undergoes an initial transient period over several cycles of the driving Alfvén wave (the wave period in this case was 6.2×10^{-6} second) as the particles acquire a steady-state energy exchange with the resonant fields. After this, a steady-state regime emerges that has residual oscillatory behavior (possibly related to the particle motions in the wave), but about a clearly defined average value.

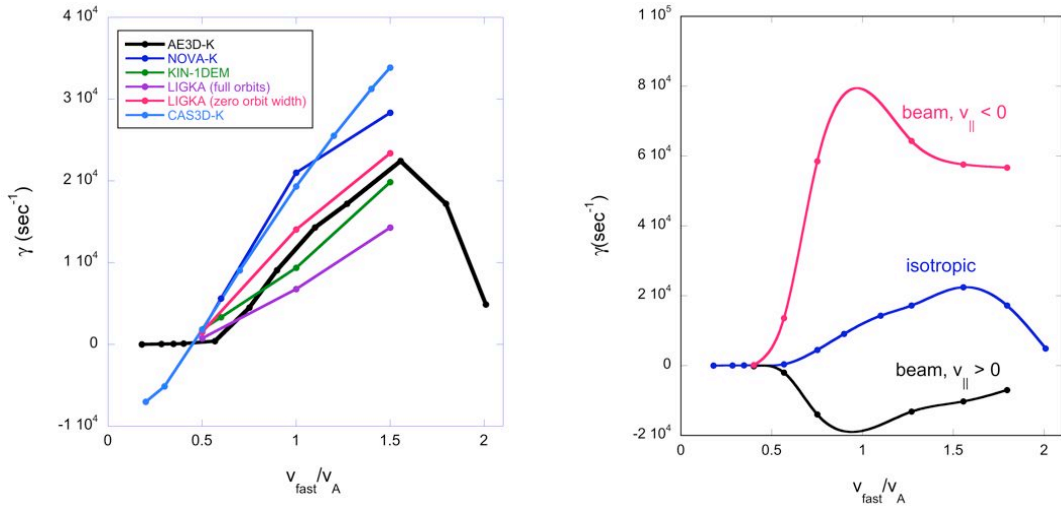


Figure 4 – (a) Comparison of growth rates vs. v_{fast}/v_A obtained from wave-particle energy transfer method (AE3D-K) for benchmark case with several other codes, (b) Comparison of growth rates for isotropic vs. beam-like particle distribution functions.

Since no obvious secular drifts in these averages appear to be present, it is reasonable to apply running time averages, as are plotted in Figure 3(a) and determine converged growth rates from these averages. In Figure 4(a) the growth rates obtained from the wave-particle energy transfer model (referred to as AE3D-K) are compared with results from the KIN-1DEM, LIGKA¹⁵, NOVA-K¹², and CAS3D-K¹⁹ codes. As can be seen, the results and scaling with v_{fast}/v_A are similar, with AE3D-K following roughly an average of the other results, except that CAS3D-K¹⁹ shows stronger damping for $v_{\text{fast}}/v_A < 0.5$. Also, AE3D-K has been extended to higher values of v_{fast}/v_A and shows a strong drop-off in its growth rate for $v_{\text{fast}}/v_A > 1.5$. Although some of this drop-off may be due to particle velocities moving out of resonance with the wave, it is also expected that a significant fraction of it is caused by FOW effects.

Figure 4(b) compares growth rates between isotropic and beam-like energetic particle distributions. In the beam case a delta function about $\mu / \varepsilon = 0$ has been used with a single direction for v_{\parallel} . Also, a single polarization (in the direction of the parallel wavenumber) for the Alfvén eigenmode has been used, which accounts for the difference between $v_{\parallel} > 0$ (stable) and $v_{\parallel} < 0$ (unstable) cases. In the unstable regime the $v_{\parallel} < 0$ beam growth rates are a factor of 3 – 6 above those for the isotropic distribution function. It is expected that this enhancement is caused by several factors: (a) the weaker variation in v_{\parallel} along the orbit trajectories for the passing beam ions, resulting in resonant particles remaining in resonance with the wave for longer times as compared to the isotropic distribution which includes a greater variation in v_{\parallel} due to the presence of passing and trapped particles; and (b) weaker FOW effects for the passing beam orbits, which generally have smaller displacements from their initial flux surfaces than the combined passing/trapped orbits that are present in the isotropic distribution.

Stellarator examples

(A) LHD

LHD is a 10 field period helical system with aspect ratio $R_0/a = 7$. An equilibrium has been selected with $R_0 = 3.7$ meters, $\langle B \rangle = 3.1$ Tesla, $i(0) = 0.33$, $i(\text{edge}) = 0.97$,

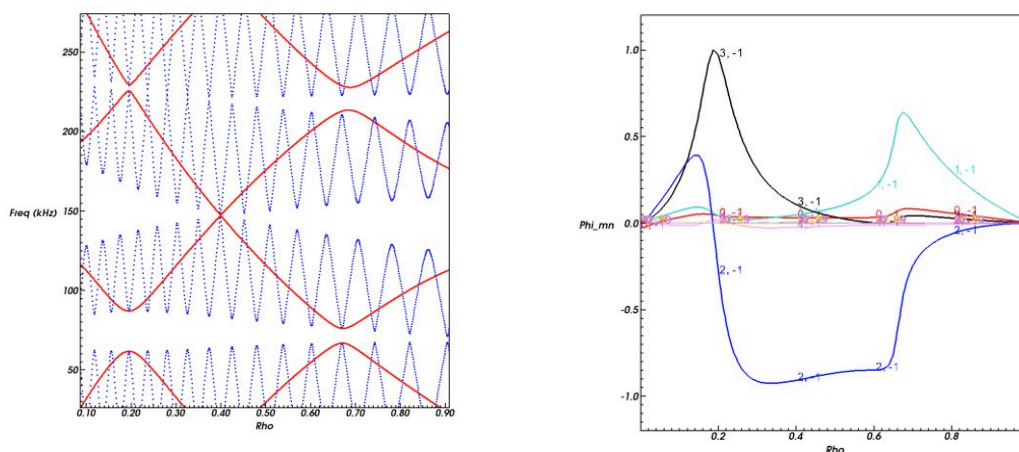


Figure 5 – (a) $n = 1$ mode family continuum gap structure, (b) TAE eigenmode in the lowest frequency gap at 74.1 kHz.

Hydrogen ions are used, with $n_{\text{fast}}(0) = 1.2 \times 10^{18} \text{ m}^{-3}$ and the ion density profile that aligns the gaps has been used, $n_{\text{ion}} = n_{\text{ion}}(0)[-i(\rho)/-i(0)]^2$, with $n_{\text{ion}}(0) = 3 \times 10^{19} \text{ m}^{-3}$. This case has been constructed for testing of this model and does not correspond to and actual experimental discharge. An $n = 1$ TAE mode was selected with a frequency of 74.1 kHz. The associated continuum gap structure and radial eigenmode structure are displayed in Figure 5. The corresponding 3D eigenmode structure is shown in Figure 6.

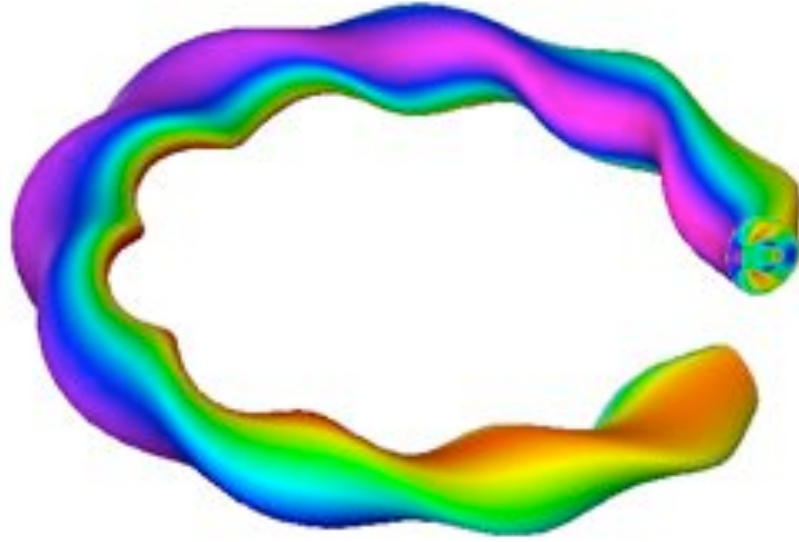


Figure 6 – LHD TAE eigenmode structure projected onto an outer flux surface.

The time-evolving growth rates for the above eigenmode driven by an isotropic Maxwellian distribution are shown in Figure 7 along with the dependence of the averages of these growth rates on v_{fast}/v_A .

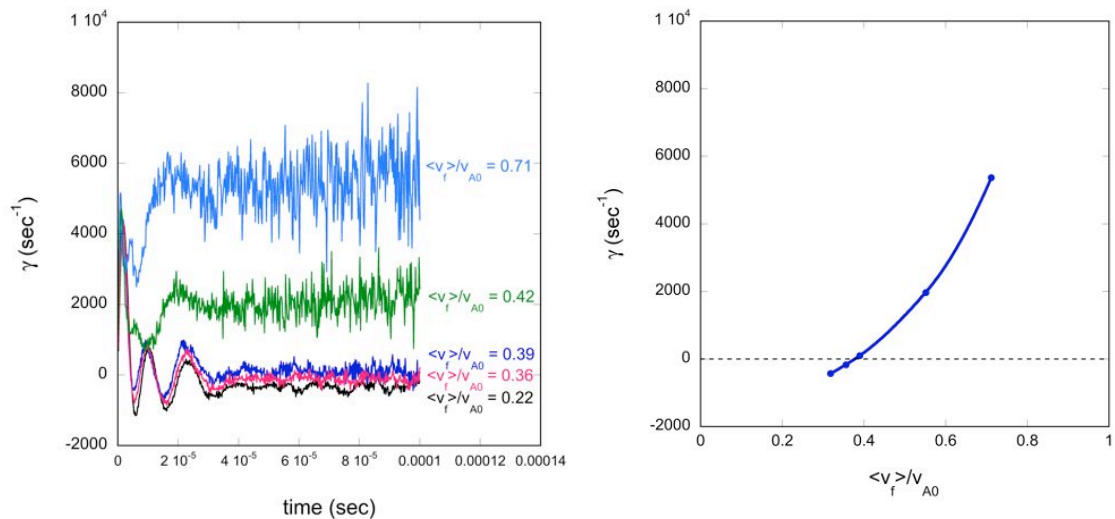


Figure 7 – (a) instantaneous growth rates for LHD $n = 1$ TAE eigenmode driven by an isotropic distribution, (b) Variation of time averaged growth rates with v_{fast}/v_A .

As can be seen, the mode begins to be unstable for $v_{\text{fast}}/v_A \sim 0.4$ and has about a factor of two lower growth rate than the previous tokamak case. In order to diagnose the regions of phase space that drive the instability, the parallel coordinates method²⁰ has been used, as shown in Figure 8.

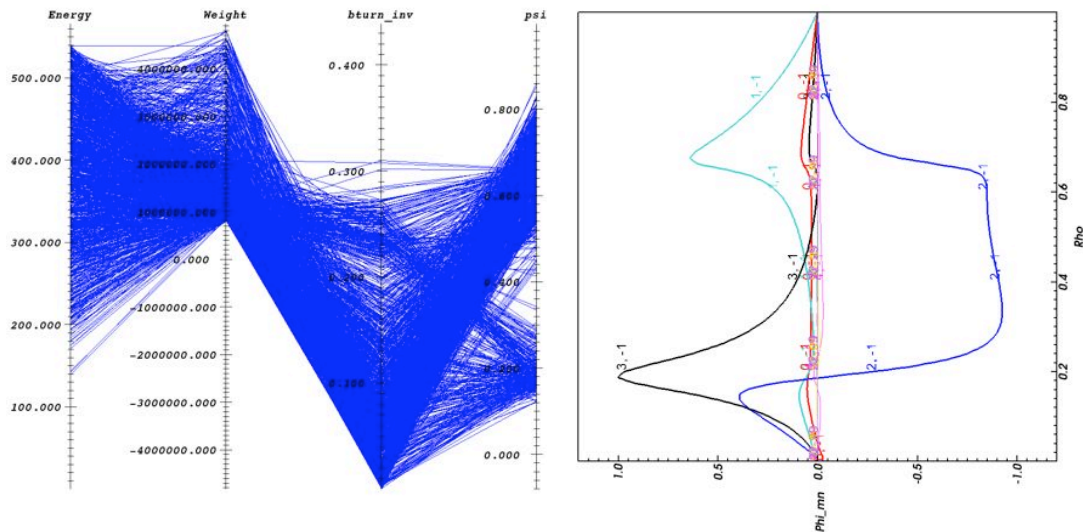


Figure 8 – Parallel coordinates plot for LHD isotropic particle distribution and alignment of flux coordinate regions with peaks in eigenmode structure.

In this plot, the particle marker coordinates of energy, contribution to the growth rate (labeled here as weight), μ / ε (labeled here as bturn_inv), and radial flux coordinate are placed on 4 vertical parallel lines. The values of these four parameters for each particle are then connected by straight lines. The density of lines then allows one to infer, for example, which classes of particles account for the instability drive. This has been emphasized in Figure 8 by restricting the lines only to those that connect to positive values on the weight axis. It can be seen that the drive arises predominantly from passing ions (passing orbits are located in the region $\mu / \varepsilon < 1/B_{\text{max}} \sim 0.22$ for this equilibrium) in the 200 to 500 keV energy range and localized in two radial regions ($0.14 < \rho < 0.3$ and $0.52 < \rho < 0.8$). Comparing these radial regions with the adjoining eigenmode radial structure indicates that the resonant destabilization is mostly coming from coupling to the $m,n = (3, -1)$ and $(1, -1)$ modes.

The dominant drive from passing ions indicated in Figure 8(a) was further tested by carrying out calculations with a beam distribution function. Results for growth rates are shown in Figure 9. As indicated in Figure 9(a), after a transient period of about 3 wave periods (one period = 1.35×10^{-5} second here) the growth rates settle into a steady state with lower noise levels than the isotropic model results of Figure 7(a). The beam model growth rates are also substantially larger than those for the isotropic model (a factor of 10 - 20) and become unstable at a lower $v_{\text{fast}}/v_A \sim 0.25$. This large difference between purely passing and isotropic distributions can be caused by several factors, including a lower degree of resonance along the trapped and transitional orbits (included in the isotropic case) as well as stronger FOW effects in the trapped populations than for the all passing case.

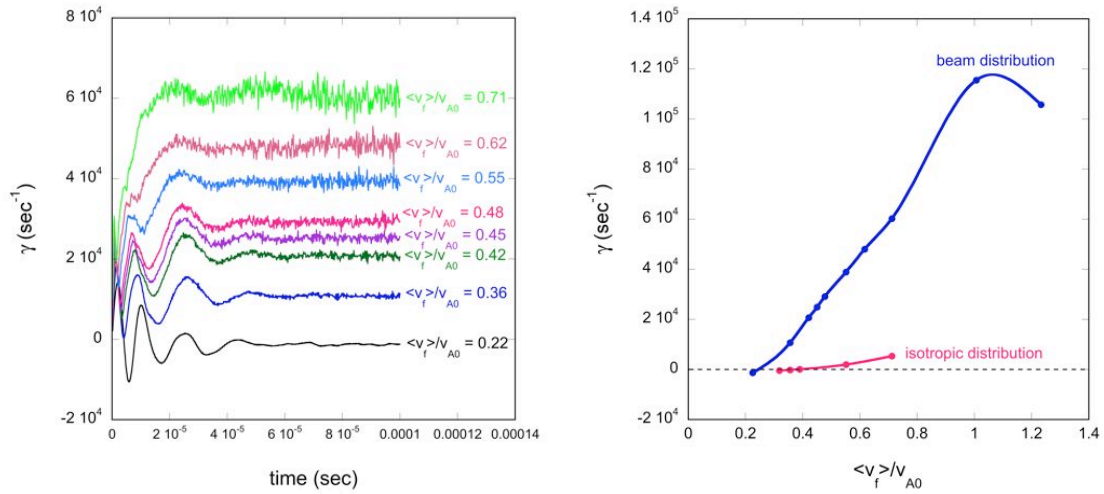


Figure 9 – (a) instantaneous growth rates for LHD $n = 1$ TAE eigenmode driven by a beam distribution, (b) Variation of time averaged growth rates with v_{fast}/v_A for isotropic and beam distributions.

(B) TJ-II

TJ-II is a 4 field period strong helical axis system with aspect ratio $R_0/a = 7.2$. An equilibrium has been selected with $R_0 = 1.5$ meters, $\langle B \rangle = 1$ Tesla, $\tilde{\kappa}(0) = 1.55$, $\tilde{\kappa}(\text{edge}) = 1.68$, Hydrogen ions are used, and a linearly decreasing ion density profile has been used, with $n_{ion}(0) = 3 \times 10^{19} \text{ m}^{-3}$. An $n=3$ dominated HAE mode was selected with a frequency of 148 kHz. The associated continuum gaps and radial eigenmode structure are displayed in Figure 10. The corresponding eigenmode structure projected onto an outer flux surface is shown in Figure 11.

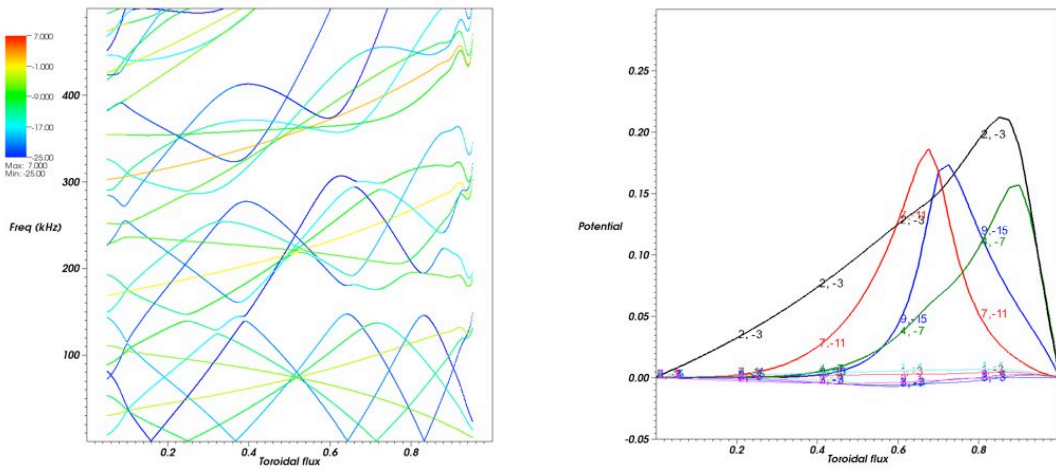


Figure 10 – (a) $n = 1$ mode family TJ-II continuum gap structure, (b) HAE 148 kHz eigenmode from the lowest frequency gap.

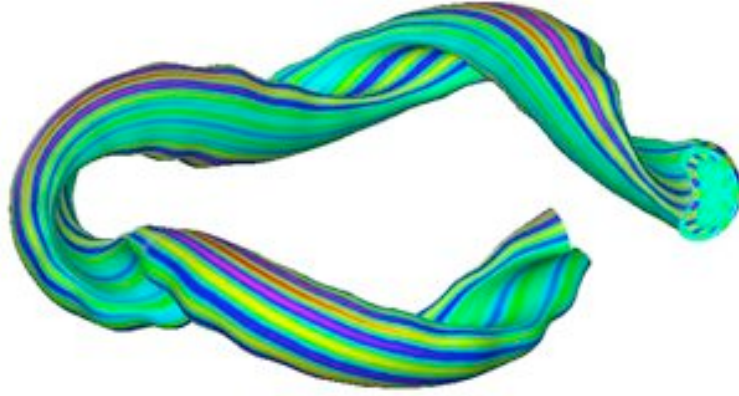


Figure 11 – LHD HAE eigenmode structure projected onto an outer flux surface.

Growth rates vs. time and v_{fast}/v_A are shown in Figure 12 for a beam distribution function based on the above HAE eigenmode.

(C) W7-AS

W7-AS is a five field period helical system with aspect ratio $R_0/a = 11.7$. An equilibrium has been selected with $R_0 = 2$ meters, $\langle B \rangle = 2.5$ Tesla, $\#(0) = 0.36$, $\#(\text{edge}) = 0.34$, Hydrogen ions are used, and a parabolic ion density profile with $n_{ion}(0) = 6 \times 10^{19} \text{ m}^{-3}$. An $m,n = 3,1$ dominated mode with a global radial structure and a frequency of 32 kHz was found which is similar to the mode observed in Ref. 1. The associated continuum gaps and radial eigenmode structure are displayed in Figure 13. The corresponding eigenmode structure projected onto an outer flux surface is shown in Figure 14.

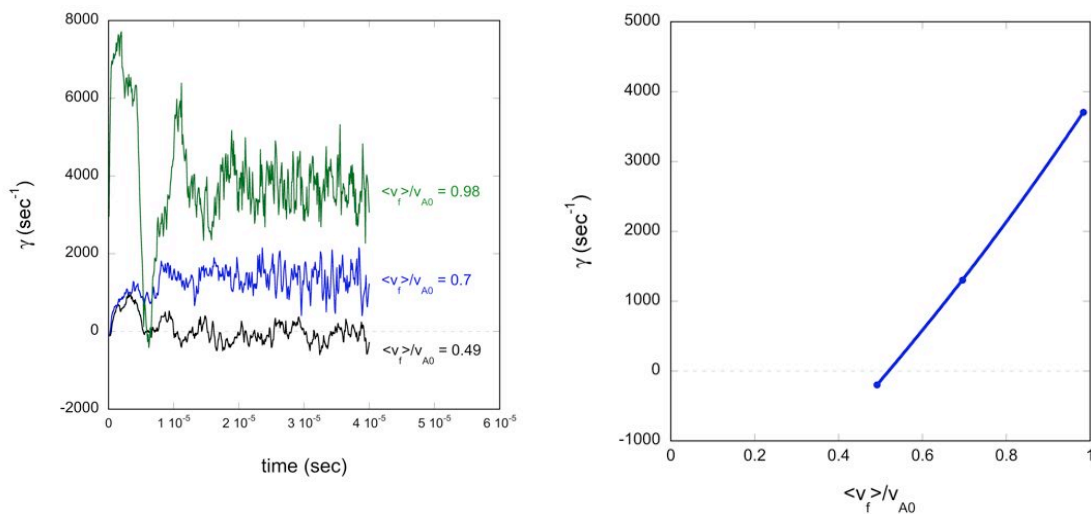


Figure 12 – (a) instantaneous growth rates for TJ-II HAE eigenmode driven by a beam distribution, (b) Variation of time averaged TJ-II HAE growth rates with v_{fast}/v_A .

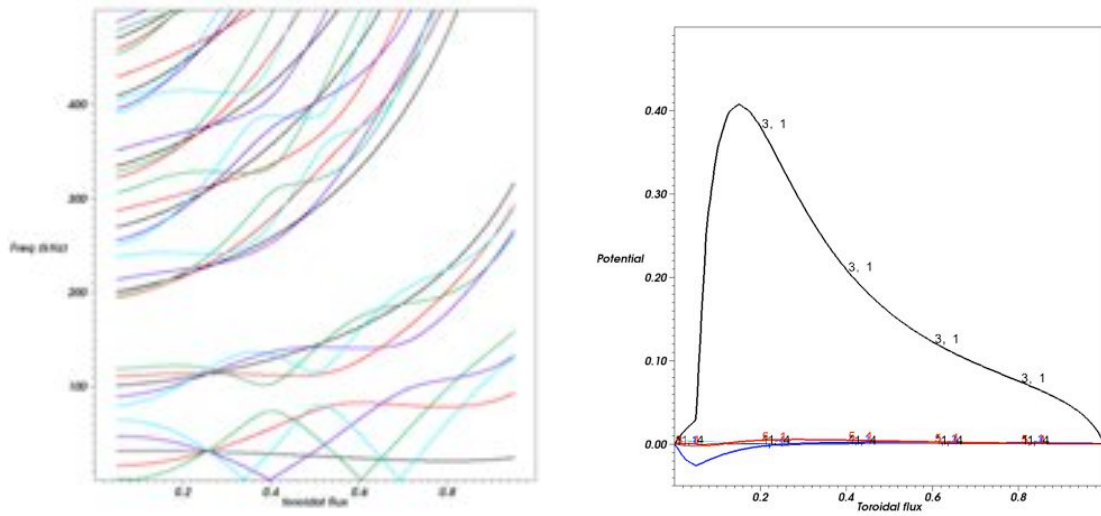


Figure 13 – (a) $n = 1$ mode family W7-AS continuum gap structure, (b) 32 kHz eigenmode below minimum of lowest $n = 1$ continuum.

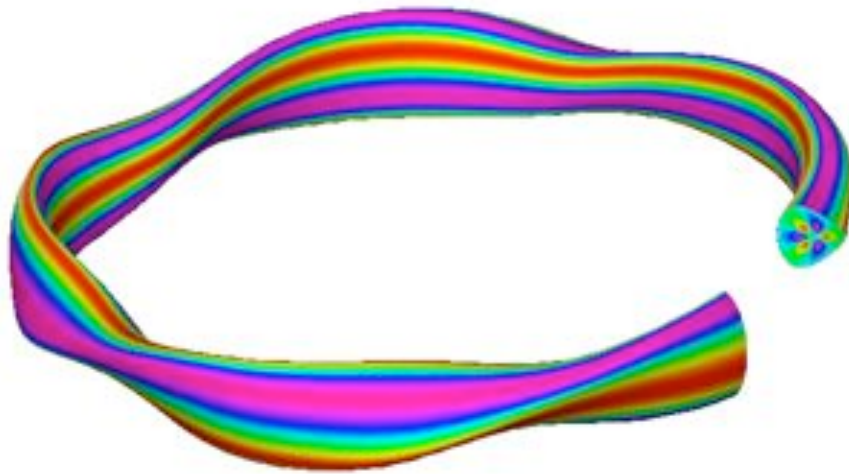


Figure 14 – W7-AS eigenmode structure projected onto an outer flux surface.

Growth rates vs. time and v_{fast}/v_A are shown in Figure 15 for a beam distribution function based on the above eigenmode. Due to the lower frequency of this eigenmode some of the instantaneous growth rates take a longer time to reach steady state (the wave period in this case was 3.1×10^{-5} second) than in the previous cases. As shown in Figure 15, due to the lack of mode coupling in this case, the growth rate shows a more rapid variation with v_{fast}/v_A than for the other configurations. The indicated range of unstable v_{fast}/v_A 's is consistent with the parameter range where an unstable mode was reported in the experiment.¹

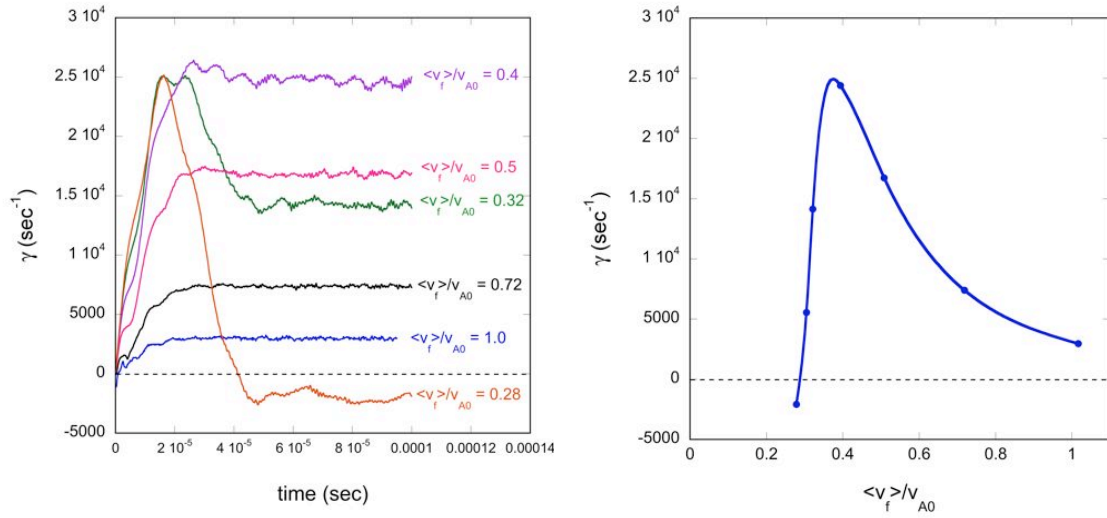


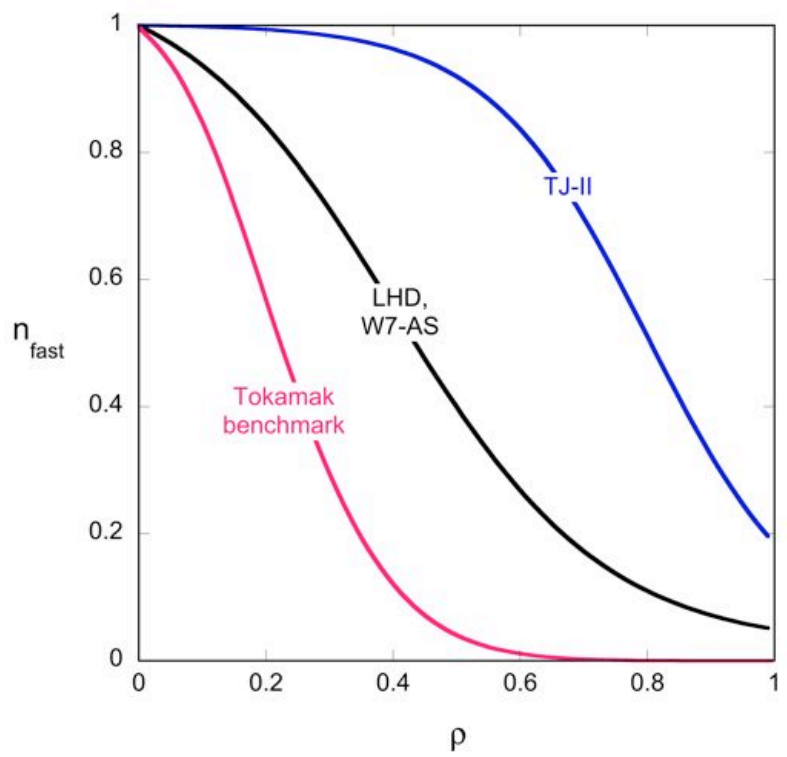
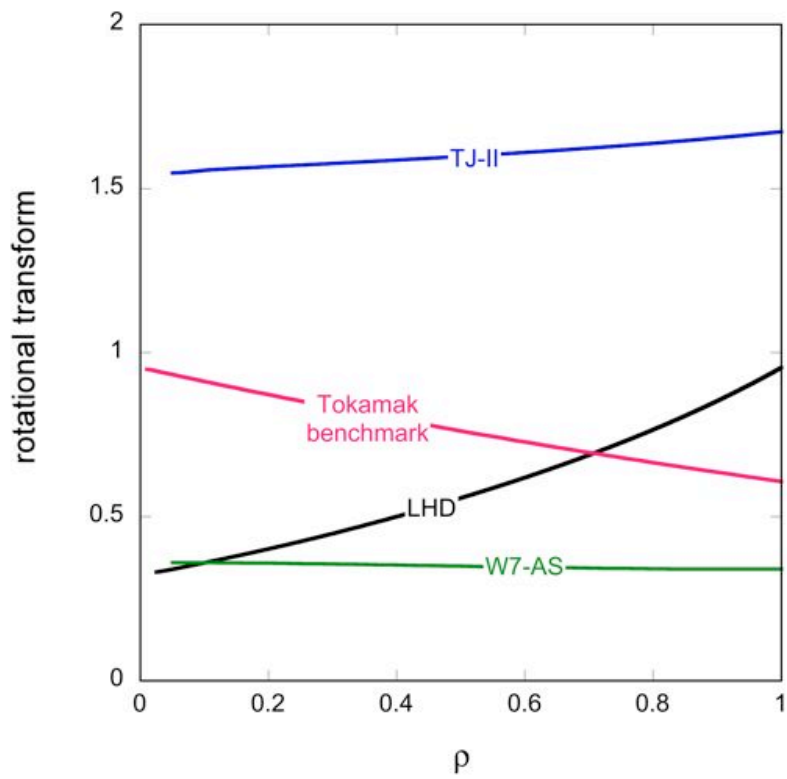
Figure 15 – (a) instantaneous growth rates for W7-AS eigenmode driven by a beam distribution, (b) Variation of time averaged W7-AS growth rates vs. v_{fast}/v_A .

Conclusions

An Alfvén wave-particle energy transfer model has been developed for addressing the linear stability properties of tokamaks and stellarators, including finite orbit width (FOW) effects. This is based on a δf particle technique that incorporates Landau resonant effects in the time domain by following particle weight evolution equations along the unperturbed particle orbits. Good agreement has been obtained with several other independent codes on a tokamak benchmark case. Applications to stellarators have indicated growth rates that become positive (unstable) in the threshold ranges of $v_{fast}/v_A = 0.25$ to 0.4 where coupling to Alfvén modes is expected. Also, when growth rates have been compared between beam and isotropic fast ion distribution functions, the beam models have been significantly more unstable, consistent with increased FOW effects from the trapped populations or due to the fact that the trapped particles are not in resonance for as large a fraction of their orbits as the passing particles. Applications of this model were given for three different stellarators (LHD, TJ-II, W7-AS). It should be applicable to a wide range of stellarator configurations as well as for tokamaks with symmetry-breaking effects.

Appendix A

The following two figures show the rotational transform profiles and fast ion density profiles that were used for the tokamak and stellarator examples.



Acknowledgements –This submission was sponsored by a contractor of the United States Government under contract DE-AC05-00OR22725 with the United States Department of Energy. The United States Government retains, and the publisher, by accepting this submission for publication, acknowledges that the United States Government retains, a nonexclusive, paid-up, irrevocable, worldwide license to publish or reproduce the published form of this submission, or allow others to do so, for United States Government purposes. One of the authors has been supported by EURATOM MOBILITY.

-
- ¹ A. Weller, D. A. Spong, R. Jaenicke, et al., Phys. Rev. Lett. **72**, 1220 (1994).
 - ² M. Isobe, K. Toi, H. Matsushita, et al. Nucl. Fusion **46**, S918 (2006).
 - ³ K. Toi, S. Yamamoto, N. Nakajima, et al. Plasma Phys. and Control. Fusion **46**, S1 (2004).
 - ⁴ R. Jimenez-Gomez, E. Ascasibar, et al., Fusion Science and Technology **51**, 20 (2007).
 - ⁵ S. Yamamoto, K. Nagasaki, Y. Suzuki, et al., Fusion Science and Technology, **51**, 92 (2007).
 - ⁶ C. Deng, D. L. Brower, B. N. Breizman, D. A. Spong, et al., Phys. Rev. Lett. 103, 025003 (2009).
 - ⁷ H. L. Berk, B. N. Breizman, H. Ye, Physics Letters A 162 (1992) 475-481.
 - ⁸ G. Y. Fu, C. Z. Cheng, and K. L. Wong, Phys. Fluids B 5 (1993) 4040.
 - ⁹ J. Candy, M. N. Rosenbluth, Nuclear Fusion, Vol.35, No.9 (1995) 1069.
 - ¹⁰ H. V. Wong, H. L. Berk, B. N. Breizman, Nuclear Fusion, Vol. 35, No. 12, pg. 1721 (1995)
 - ¹¹ T. Fulop, M. Lisak, et al., Plasma Phys. Control. Fusion 38 (1996) 811–828.
 - ¹² N.N. Gorelenkov, C. Z. Cheng, G. Y. Fu, Physics of Plasmas Vol. 6, No. 7 (1999) 2802.
 - ¹³ S. E. Sharapov, A. B. Mikhailovskii, G. T. A. Huysmans, Phys. Plasmas, Vol. 11, No. 5, (2004) 2287.
 - ¹⁴ F. Zonca, L. Chen, Plasma Phys. Control. Fusion 48 (2006) 537–556.
 - ¹⁵ Ph. Lauber, S. Günter, A. Könies, S.D. Pinches, Journal of Computational Physics 226 (2007) 447–465.
 - ¹⁶ Ya.I. Kolesnichenko, V.V. Lutsenko, A. Weller, et al., Nucl. Fusion 46 (2006) 753–769.
 - ¹⁷ C. Nührenberg, Phys. of Plasmas **6**, 137 (1999).

¹⁸ D. A. Spong, Y. Todo, L. A. Berry, et al. , paper TH/3-4, 22nd IAEA Fusion Energy Conference, Geneva, Switzerland (Oct., 2008); also, D. A. Spong, E. D’Azevdo, Y. Todo, submitted to Phys. Plasmas (2009).

¹⁹ A. Könies, Phys. Plasmas 7, 1139 (2000).

²⁰ C. Jones, K.-L. Ma, S. Ethier, W.-L. Lee, Computing in Science and Engineering, Vol. 10, No. 4, pg. 20 (July/August, 2008).